Elongation and burst of axisymmetric viscoelastic droplets: A numerical study

J. Beaucourt, T. Biben, and C. Verdier
Laboratoire de Spectrométrie Physique, CNRS, Université Joseph Fourier (Grenoble I), Boîte Postale 87, Saint-Martin d'Hères, 38402 Cedex, France
(Received 27 October 2004; revised manuscript received 22 February 2005; published 28 June 2005)

The dynamics of elongation and burst of an isolated viscoelastic drop are investigated numerically in the special case of a viscosity ratio $\lambda=1$. We show that the burst threshold is not affected by viscoelasticity itself, whereas the stationary drop morphology is. A dimple at the tips of the drop can even be observed when elastic effects are large. The burst dynamics is very sensitive to the presence of viscoelasticity: at low elasticity burst is slowed down while for large elasticity levels it becomes even faster than the Newtonian situation.

DOI: 10.1103/PhysRevE.71.066309 PACS number(s): 47.55.Dz, 47.50.+d, 83.50.Lh, 47.11.+j

The pioneering works of Taylor [1] opened the way to a wide series of studies of elongation and breakup of Newtonian droplets. These original contributions led to an analytical expression for the deformation of an isolated Newtonian droplet in a Newtonian matrix, in the limit of small deformations. Those results have been progressively refined and extended [2,3]. A general overview of the dynamical behavior of such droplets in a large variety of flows can be sketched. This system is entirely characterized by two dimensionless numbers, the capillary number Ca, which compares the applied stress to the resistance of the drop due to surface tension effects, and the viscosity ratio between the internal and external fluids λ. Depending on the value of these parameters, several behaviors can be observed, and we refer the interested reader to the reviews on these questions by Rallison [4] and Stone [5] and references therein. Due do its fundamental importance in the description of the rheological properties of multiphase flows, several studies have been devoted to the presence of interfaces in dilute suspensions, by Oldroyd [6,7] and then by Palierne, who extended these studies to the viscoelastic case [8]. Although these important studies are limited to small deformations due to the highly nonlinear and free boundary nature of the problem, their predictions have been successfully compared to experimental results in the case of uniaxial elongational flows [9]. The case of viscoelastic droplets is more complicated since viscoelasticity implies retarded effects due to energy storage. This energy storage is characterized by at least an extra parameter, a relaxation time, but the actual situation is much more complicated. Several models indeed exist, which can contain as much as eight independent parameters [10]. This feature reflects the complexity of the experimental situation where the presence of the precise chemical structure of the polymers can strongly affect their viscoelastic response. For the sake of simplicity we shall restrict here the discussion to an Oldroyd-B fluid, for which viscoelasticity is accounted for by two extra parameters: a relaxation time describing the elastic storage and a viscosity.

Only a few numerical attempts have been made so far to investigate the droplet dynamics in an elongation flow. Maffettone and Greco used an asymptotic expansion for small capillary numbers to determine the droplet shape and stability curves [11]; they showed that elasticity has little or no effect on the critical capillary number. Ramaswamy and Leal [12] solved the complete free boundary problem in the steady regime using the Chilcott-Rallison (CR) model. They showed that the effect of viscoelasticity is rather complicated because of the combined effects of viscoelastic stresses at the tips and the viscous forces due to the change in the flow within the droplet.

In this paper, we focus on the dynamical behavior of an isolated droplet containing a dilute suspension of polymers, the drop being subjected to a hyperbolic flow. This is the natural extension of a previously published work on the elongation and breakup of a Newtonian drop in an extensional flow [13], which allowed us to validate a phase field description of the interface. Classical numerical methods [finite element method (FEM) or boundary element method (BEM)] have been used for this problem in the case of pure elongation [14,15], but to our knowledge these methods have never been applied to the breakup situation itself.

Section I is devoted to the governing equations and the relevant parameters; we also briefly describe the phase field approach we shall use (the Appendix is devoted to the more technical aspects of the numerical scheme). The phase field approach has already been used for the description of other physical mechanisms, from the original works by Collins and Levine [16] for the simulation of diffusion-limited crystal growth, extended to the problem of dendritic growth by Kobayashi [17], and latter by Karma and Rappel [18] to stress-induced instabilities in solids by Kassner and Misbah [19]. In fluid mechanics, Hele-Shaw instabilities [20,21], Marangoni convection [22], vesicles dynamics [23], or polymer blends [24] are examples of applications of this method. The next two sections are devoted to the study of the elongation process when the applied constraint is increased: while the steady states are the subject of Sec. II, we consider the burst itself in Sec. III, when the applied elongation rate is too high for the drop to resist. Although the local viscoelastic stress can hardly be measured experimentally, the numerical approach allows us to monitor its localization quite easily, and is thus a useful complement to experimental observations. We shall focus our analysis on this particular point and discuss the observed behaviors.

I. MODEL

We consider a three-dimensional (3D) axisymmetric viscoelastic droplet (See Fig. 1) of initial radius R suspended in

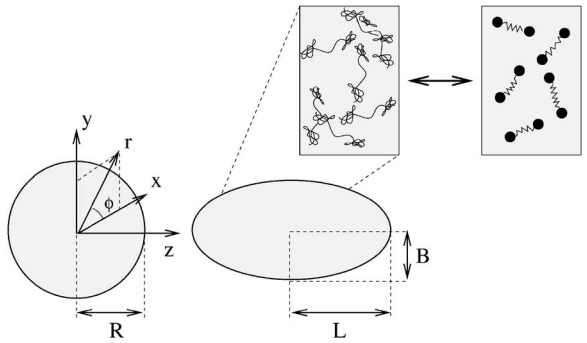

FIG. 1. Sketch of the system. The initial radius of the drop is denoted by R and the long (small) axis by $L(B)$. The polymers inside the drop are modeled by spherical beads connected by springs (Rouse model).

a viscous medium with viscosity $\eta_{s,o}$, and submitted to a hyperbolic flow,

$$\mathbf{v}_i = (-\dot{\gamma}/2r, 0, \dot{\gamma}z) \tag{1}$$

[in cylindrical coordinates (r, ϕ, z), r and ϕ are the radial and azimuthal coordinates, respectively, and z is along the extension axis], with $\dot{\gamma}$ the extension rate.

The drop itself is a polymer solution in a viscous solvent with viscosity $\eta_{s,i}$. The polymer contribution to the global stress is described here by an Oldroyd-B equation, which contains only two parameters: a relaxation time τ which can be interpreted as the typical time scale for the polymers to relax, and a viscosity η_p. This kind of model thus includes the basic ingredients of energy storage and retarded effects related to viscoelasticity. It must be noted that nonlinear effects such as a power law relation between the polymer viscosity and the local shear rate are not accounted for by this model, although they can have practical importance at large shear rates [10]. The Oldroyd-B equation is indeed known to describe correctly the dynamical behavior of dilute polymeric solutions [for example, the so-called "Boger fluids" made of dilute polyisobutylene in polybutene (PIB/PB) for shear rates between 0.1 and 10 s^{-1} [25]]. Typical properties of the Oldroyd-B model are a constant shear viscosity and a nonzero first normal stress difference in shear flows. In elongation, it predicts strain hardening above a critical extension rate $(2\dot{\gamma}\tau=1)$. This constitutive equation relates implicitly the polymer stress tensor to the applied deformations due to the local flow in the following way:

$$\overset{\nabla}{\tau}\boldsymbol{\sigma}_p + \boldsymbol{\sigma}_p = \eta_p(\boldsymbol{\nabla}\mathbf{v} + \boldsymbol{\nabla}\mathbf{v}^T). \tag{2}$$

Here, τ is the typical relaxation time of the polymers, η_p is the zero-shear rate viscosity of this phase, $\mathbf{v}$ is the local velocity field, and superscript T denotes the transposition of the tensor. The total viscosity of the drop will then be given by $\eta_{s,i}+\eta_p$. The superscript $\overset{\nabla}{-}$ denotes the upper convective time derivative, and is given explicitly by

$$\overset{\nabla}{\boldsymbol{\sigma}}_p = \partial_t\boldsymbol{\sigma}_p + \mathbf{v}\cdot\boldsymbol{\nabla}\boldsymbol{\sigma}_p - \boldsymbol{\nabla}\mathbf{v}^T\cdot\boldsymbol{\sigma}_p - \boldsymbol{\sigma}_p\cdot\boldsymbol{\nabla}\mathbf{v}. \tag{3}$$

This macroscopic equation can be derived from more microscopical considerations [26] by considering a model of beads connected by a thermal spring, a crude model for a polymer in a solvent. The polymers are thus assumed to be monodisperse and to have a single relaxation time. The coupling between the "polymers" and the surrounding viscous fluid is described by a drag force proportional to the relative velocity of the beads and the fluid. This approach allows us to relate the macroscopic coefficients τ and η_p to the polymer properties, such as the radius of gyration R_g, the polymer concentration ν, and the thermal energy k_BT. The resulting dependence for τ and η_p is $\tau \propto R_g^3\eta_{s,i}/(k_BT)$ and $\eta_p \propto \eta_{s,i}\nu R_g^3$ [26]. The Newtonian limit corresponds either to $\tau=0$ or to $\eta_p=0$. For a given temperature and solvent viscosity the latter condition corresponds to a vanishing volume fraction of polymers $\nu R_g^3=0$ while the former is associated with a cancellation of the radius of gyration $R_g=0$ only (and the corresponding polymers reduce to classical molecules). These two conditions are thus of different physical origin and the polymer concentration can formally be canceled by dilution at a fixed value of the radius of gyration (i.e., at fixed relaxation time). The relaxation time alone is thus not a direct characterization of the viscoelasticity of the polymer solution. Another way to cancel the relaxation time is to increase temperature: in that case, the Brownian forces dominate the viscous drag and the polymers decouple from the surrounding fluid.

The interfacial energy between the drop and the suspended medium is called Σ. This parameter is affected by the possible adsorption of polymers at the interface, resulting in a Marangoni effect which could have profound consequences on the drop behavior such as tip streaming [5]. This coupling is not included in our study. Including the mass density ρ of the fluids (we consider here neutrally buoyant droplets, so the density inside and outside are the same), we can construct five dimensionless parameters which describe the system entirely:

$$\mathrm{Re} = \frac{\rho R^2\dot{\gamma}}{\eta_{s,o}}, \text{ the Reynolds number,}$$

$$\mathrm{Ca} = \frac{\eta_{s,o}\dot{\gamma}R}{\Sigma}, \text{ the capillary number,}$$

$$\mathrm{De} = \frac{\tau\Sigma}{\eta_{s,o}R}, \text{ the Deborah number,} \tag{4}$$

$$\lambda_s = \frac{\eta_{s,i}}{\eta_{s,o}}, \text{ the (solvent)/(solvent) viscosity ratio,}$$

$$\lambda_p = \frac{\eta_p}{\eta_{s,o}}, \text{ the (polymer)/(solvent) viscosity ratio.}$$

These parameters can be estimated for Boger fluids using typical values as discussed in [25]. We shall first estimate the Reynolds number that compares inertial to viscous stresses. If we consider a 100 μm drop suspended in a medium with viscosity $\eta_{s,o}\sim 1$ Pa s (like glycerol), the mass density of

both fluids being of the order of $\rho \sim 10^3$ kg m^{-3}, the Reynolds number can be estimated to $\mathrm{Re} \sim 10^{-5}$ for a shear rate $\dot{\gamma} \sim 1$ s^{-1}. Inertia can thus be neglected and we shall use the Stokes approximation in the following. Ca compares the resistance of the drop (due to surface tension effects) to the applied stress: a large capillary number corresponds to a highly deformable drop. This is the first key control parameter of this study. With a typical $\Sigma \sim 10^{-3}$ N m^{-1} we get Ca ~ 0.1. The second essential parameter is the Deborah number characterizing the elastic effects in the internal fluid: the larger the De, the higher the viscoelastic effects. Using a typical value $\tau \sim 1$ s, the Deborah number is $\mathrm{De} \sim 10$. Finally, the two viscosity ratios will be chosen such that $\lambda = \lambda_s + \lambda_p = 1$ and $\lambda_s = \lambda_p = 0.5$ in the following, essentially to reduce the parameter space dimension. Of course these dimensionless parameters can be combined to form alternative parameters, like the Weissenberg number $\tau\dot{\gamma}$ which can be used instead of the Deborah number. While the Deborah number compares the relaxation time of the polymers to the capillary time, and thus characterizes the viscoelasticity of the droplet intrinsically (whatever the applied flow), the Weissenberg number, on the contrary, compares the viscoelastic time to the applied deformation rate. Our preference for the Deborah number is based on the type of experiment we wish to model: we apply an increasing elongation rate to a given drop, which corresponds to a fixed Deborah number and an increasing capillary number.

In order to use dimensionless equations, we rescaled the time variable by the typical relaxation time of the drop $t_{drop} = \eta_{s,o} R/\Sigma$ and the length by its initial radius R. The governing equations are thus given by

$$\begin{aligned} \nabla \cdot (\boldsymbol{\sigma}_p + \boldsymbol{\sigma}_{s,i}) - \nabla P_{in} = 0 \quad \text{inside}, \\ \nabla \cdot \boldsymbol{\sigma}_{s,o} - \nabla P_{out} = 0 \quad \text{outside}. \end{aligned} \tag{5}$$

$\boldsymbol{\sigma}_{s,i}$ and $\boldsymbol{\sigma}_{s,o}$ are the Newtonian contributions to the stress, respectively, inside and outside the drop. They are simply related to the local deformation rate in the fluid by a linear relation $\boldsymbol{\sigma}_{s,i} = \lambda_s(\nabla \mathbf{v} + \nabla \mathbf{v}^T)$ (and $\boldsymbol{\sigma}_{s,o} = \nabla \mathbf{v} + \nabla \mathbf{v}^T$ for the outer fluid). The appropriate dimensionless boundary conditions at the drop interface ∂V are given by

$$\begin{aligned} \mathbf{v}_{in}|_{\partial V} \cdot \hat{\mathbf{t}} = \mathbf{v}_{out}|_{\partial V} \cdot \hat{\mathbf{t}}, \\ \mathbf{v}_{in}|_{\partial V} \cdot \hat{\mathbf{n}} = \mathbf{v}_{out}|_{\partial V} \cdot \hat{\mathbf{n}}, \\ \hat{\mathbf{n}} \cdot (\boldsymbol{\sigma}_{s,o} - P_{out} I_3)|_{\partial V} = \hat{\mathbf{n}} \cdot (\boldsymbol{\sigma}_p + \boldsymbol{\sigma}_{s,i} - P_{in} I_3) \cdot \hat{\mathbf{n}}|_{\partial V} - (\kappa_1 + \kappa_2)\hat{\mathbf{n}}, \end{aligned} \tag{6}$$

with κ_1 and κ_2 the two main local curvatures of the drop (positive for a sphere) [27] and I_3 the three dimensional unit tensor. The first equation describes the continuity of the tangential velocity field across the interface (no slip condition), the second one expresses the absence of flow across the interface, and the last one describes the continuity of the total stress. The tangential stress is continuous, but the normal stress presents a jump equal to the local curvature of the interface (surface tension is absorbed in the scaling), according to the Laplace law. The local incompressibility of the fluid writes

$$\nabla \cdot \mathbf{v} = 0. \tag{7}$$

As mentioned previously, the polymers will be described with the Oldroyd-B equation (2). In dimensionless units we have

$$\mathrm{De} \overset{\nabla}{\boldsymbol{\sigma}}_p + \boldsymbol{\sigma}_p = \lambda_p (\nabla \mathbf{v} + \nabla \mathbf{v}^T). \tag{8}$$

This set of equations is highly singular due to the free boundary nature of the problem and to the possible topological changes in the drop shape. Recently, a phase field approach has been developed to model the deformation and breakup of a Newtonian drop [13]. The method has been shown to be quantitative in that limit. We refer the interested reader to the Appendix for further details concerning the numerical implementation of the method in the case of viscoelastic droplets. The main advantage of the method is the simplicity of its numerical implementation. The boundary conditions at the interfaces are accounted for without any complicated front tracking procedures. Basically, the method is based on a regularization of the interfacial profile, which is described by a Ginzburg-Landau-like order parameter field θ. As a result, all the singularities associated with the interfaces are removed in this description, and we simply end up with diffusionlike problems in the whole space. Obviously, such a regularization procedure introduces an extra length scale, the interfacial width, which produces a natural cutoff at small scales. This cutoff is chosen in practice to match the lattice spacing of the resolution mesh. It is thus not an important restriction. To study small scale effects, such as self-similarity laws during the breakup [28–31], or filament formations [32,33], more precise numerical schemes are, however, preferable.

We use the prescription that $\theta < 0$ inside the drop and $\theta > 0$ outside. In practice we set $\theta = \pm 1$ far away from the interface, and force its variation across the interface to be of the tanh-like form. Although this kind of profile can easily be generated initially [34], a pure advection of this profile, consistent with the boundary conditions (6), does not preserve the tanh shape. A restoring term thus has to be added to advection to enforce the tanhprofile across the interface,

$$\frac{\partial \theta}{\partial t} + \mathbf{v} \cdot \nabla \theta = \frac{1}{\Gamma}\{\theta(1 - \theta^2) + \epsilon^2(\Delta\theta - 2c[\theta]|\nabla \theta|)\} \tag{9}$$

with $c[\theta]$ the local mean curvature of the field and Γ a relaxation time. While the left hand side corresponds to advection, the right hand side is the restoring term. This contribution is made of two parts. The first one comes from the functional minimization of a Ginzburg-Landau-like free energy $\mathcal{F}$,

$$\frac{\delta \mathcal{F}}{\delta \theta} = \theta(1 - \theta^2) + \epsilon^2 \Delta \theta \tag{10}$$

with $\mathcal{F} = \int \{(1-\theta^2)^2/4 + \epsilon^2(\nabla\theta)^2/2\} d\mathbf{r}$. This term enforces a tanh-like profile for the field θ at the interface, with a sharp variation zone centered on 0 (which will define the interface

locus) and of width $\epsilon\sqrt{2}$. In order to make the numerical scheme insensitive to ϵ up to first order [20,21], a corrective term $-2\epsilon^2 c[\theta]|\nabla\theta|/\Gamma$ is added into Eq. (9) that prevents nonphysical drifts to occur. Finally, Γ is chosen such that the relaxation toward this profile is faster than any other physical process in the system. In that case, the interface can be considered to be purely advected by the flow.

The curvature field can be constructed from the normal vector field, i.e., normal to the isosurfaces of θ: $\hat{\mathbf{n}} = \nabla\theta/|\nabla\theta|$. The mean curvature is defined by $c[\theta] = \nabla\cdot\hat{\mathbf{n}}/2$ ($c=+1$ for a unit sphere). Finally, we can construct a regularized Dirac function centered on the interface

$$\delta_\theta(\mathbf{r}) = \frac{|\nabla\theta|}{2}. \tag{11}$$

The factor $1/2$ ensures the normalization of this function across the interface. The Stokes equations (5) are rewritten as

$$\nabla\cdot\left(\boldsymbol{\sigma}_{s,i}\frac{1-\theta}{2} + \boldsymbol{\sigma}_{s,o}\frac{1+\theta}{2} + \boldsymbol{\sigma}_p\right) - \nabla P - c[\theta]\nabla\theta = \mathbf{0}. \tag{12}$$

The boundary conditions (6) are automatically satisfied thanks to the continuity of all the fields involved. The momentum equation is solved using a relaxation method, introducing an auxiliary Reynolds number Re_n of typical order 10^{-2} in our case, which is compatible with the Stokes approximation. Finally, the dynamical equations to be solved are given by

$$\partial_t\theta = -\mathbf{v}\cdot\nabla\theta + \frac{1}{\Gamma}\{\theta(1-\theta^2) + \epsilon^2(\Delta\theta - 2c[\theta]|\nabla\theta|)\},$$

$$\mathrm{Re}_n\partial_t\mathbf{v} = \nabla\cdot\left(\frac{1-\theta}{2}\boldsymbol{\sigma}_{s,i} + \frac{1+\theta}{2}\boldsymbol{\sigma}_{s,o} + \boldsymbol{\sigma}_p\right) - \nabla P - c[\theta]\nabla\theta, \tag{13}$$

$$\mathrm{De}\frac{1-\theta}{2}^{\nabla}\boldsymbol{\sigma}_p = -\boldsymbol{\sigma}_p + \lambda_p\frac{1-\theta}{2}(\nabla\mathbf{v} + \nabla\mathbf{v}^T),$$

$$\nabla\cdot\mathbf{v} = 0,$$

with the appropriate applied elongation flow (1). Note that in the $\epsilon\to 0$ limit, θ becomes an indicator function (-1 inside the drop and $+1$ outside), the constitutive equation thus reduces to $\boldsymbol{\sigma}_p = 0$ outside the drop, as expected since there is no polymer there.

II. STEADY SHAPES

As a routine test of the method, we have set the relaxation time to 0 (De=0, Newtonian drop) and have plotted the stationary elongation $D=(L-B)/(L+B)$ as a function of Ca, when a steady state exists. In that limit, Taylor's result for small deformations [1] should be recovered,

$$D = \frac{3}{2}\left(\frac{19\lambda+16}{16\lambda+16}\right)\mathrm{Ca}, \tag{14}$$

where the prefactor $3/2$ accounts for the 3D elongational flow considered [4]. We can see in Fig. 2 that it is indeed the case in the limit of vanishing Ca. The order Ca^2 theory of Barthès-Biesel and Acrivos [3] is plotted also and is seen to compare very well with our numerical findings.

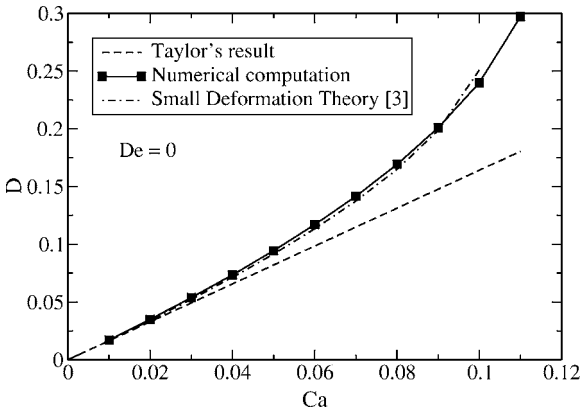

FIG. 2. Comparison between our numerical computation, the linear analysis of Taylor and the small deformation theory of Barthès-Biesel and Acrivos [3]. Here De=0 and $\lambda=1$ (no viscosity contrast).

Viscoelastic effects are obtained by increasing the Deborah number progressively. Figure 3 shows the drop deformation as a function of Ca for various Deborah numbers. The drop deformation is reduced by the presence of polymers and above a critical value of Ca (typically between 0.11 and 0.12 for all the considered values of the Deborah number), the stationary state disappears (the burst transition) and the drop breaks, as will be discussed in the next section. The shapes corresponding to Ca=0.1125 have been indicated in Fig. 3 for De=0 and 10, showing that although the deformation (as defined by D) is weaker for viscoelastic droplets, the overall shape is strongly affected by viscoelasticity. These features have been already observed in the numerical studies by Hooper *et al.* [14,15], with approximately the same order of magnitude, and by Ramaswamy and Leal [12], using the CR model.

In Fig. 4 we present the steady shape of the drop for various Deborah numbers; a curvature inversion takes place along the elongation axis in the case of the viscoelastic drop. Since L corresponds to the half length of the drop along the

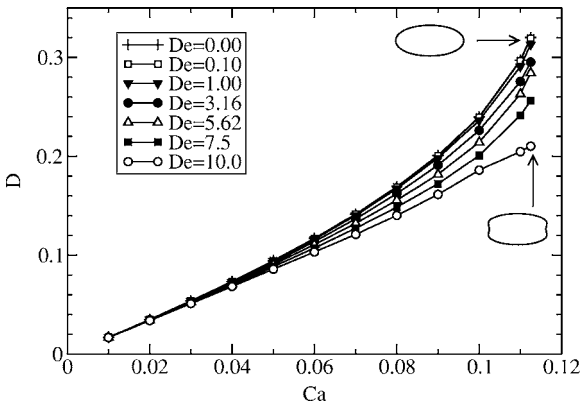

FIG. 3. Influence of viscoelasticity. The Deborah number has been varied between 0 (Newtonian) and 10. The shapes corresponding to De=0 and 10 are indicated for Ca=0.1125.

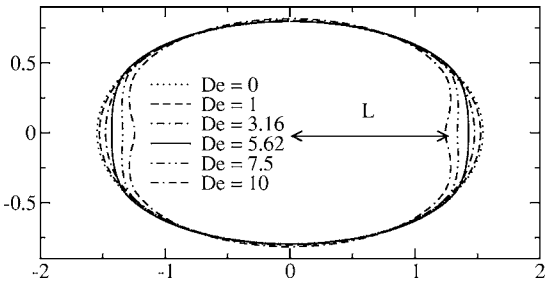

FIG. 4. Drop stationary shapes for Ca=0.1125 and increasing Deborah numbers. The tip flattens and its curvature can even be inverted for De$\geqslant$7.5. All the shapes correspond to the same volume $4\pi/3$.

axis, as depicted in Fig. 4, the deformation "*D*" is underestimated for De=10 giving the particular shape of the deformation curve presented in Fig. 3.

A plot of the mean curvature of the drop at its end, along the elongation axis, clearly illustrates this effect in Fig. 5. We observe that all the curves (for different De) collapse and tend towards the value +1 for a vanishing Ca, as expected since the drop shape remains essentially spherical in that limit, with $L \sim B \sim 1$. For small values of De, this curvature increases with Ca, showing the growing effect of the applied elongation. But above a certain value of De, between 3 and 5, this behavior is reversed and the curvature decreases with Ca. For De$\geqslant$7.5, it even becomes negative, and the rapidly decreasing slope is in favor of a cusp formation.

It is interesting to discuss in more detail the results obtained with the CR model [12]. This model is indeed a modified version of the Oldroyd-B model that suppresses some pathologies associated with it. The Oldroyd-B model is known to present some inconsistencies in hyperbolic flows for homogeneous unbounded systems, and it can be shown that the elongational viscosity diverges when $\dot{\gamma}\tau$ (which would correspond to CaDe here) reaches 1/2. This divergence is essentially due to the linearity of the springs considered in the Oldroyd-B model that does not prevent a "polymer" dumbell to extend infinitely at a finite elongation rate. The CR model introduces a nonlinearity associated with the spring constant, which is assumed to diverge as $1/[1-(x/L)^2]$ with x the actual length of the spring and L the polymer length (FENE dumbells). The Oldroyd-B model is

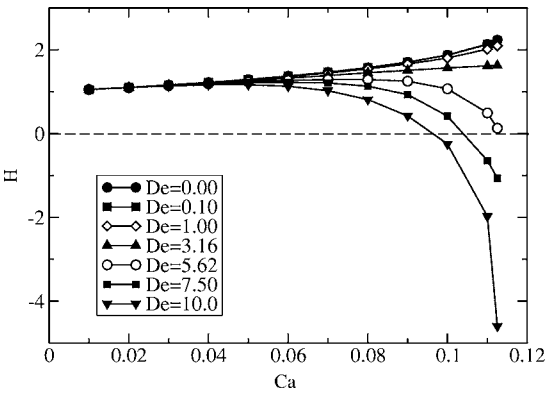

FIG. 5. Mean curvature at the tip.

recovered when $L^2 \to +\infty$. To compare our results with [12] we considered their maximum value $L^2=600$, for which Deborah numbers as large as De=10 and even De=20, with our definition, have been probed with Ca=0.1. Although the comparison is difficult since the polymer concentration is an order of magnitude lower in [12] than in our study, the observed behavior is similar, and a cancellation of the curvature at the tip can even be observed. Unfortunately, their numerical scheme could not provide solutions for nonconvex shapes and they could thus not observe the dimple formation. Although we use the Oldroyd-B model, the similarity of our results and the data obtained in [12] shows that we remain in a region where the two models are comparable (i.e., below the singularity). We are comforted further in this belief by the stability of the relaxation dynamics. All the presented shapes correspond to stable solutions, and the pathology of the Oldroyd-B model is not observed for the Deborah numbers we considered, even when $\dot{\gamma}\tau \geqslant 1/2$. We are indeed never in a situation corresponding to a steady unbounded elongational flow inside the droplet for which the pathology develops. The initial state corresponding to a pure elongational flow is unsteady, and the polymers are at rest, corresponding to a Newtonian regime. In the steady regime we can expect elongational flows to exist in the vicinity of the stagnation points, but we shall see that these points correspond to a very weak local elongation rate. We thus expect the dimple to be a physical effect. To understand the dimple formation, various quantities can be measured among which the local viscoelastic stress and the local elongation rate provide complementary informations. The viscoelastic stress is located in regions where polymers are elongated; this elongation, however, applies important constraints to the flow resulting in a reduction of its intensity.

This screening of the flow can become important in regions where polymers spend a long time, for example in the vicinity of a stagnation point like the tip of the drop [12]. On the contrary, the local elongation rate is large in regions of the flow where polymers spend a short time. A plot of these quantities is shown in Fig. 6. Before discussing this figure, it is worth introducing more precisely the various quantities presented. The flow lines are plotted in the first column of Fig. 6; they correspond to the isocontours of the streamfunction ψ defined by $\mathbf{v}=\boldsymbol{\nabla}\times(\psi\mathbf{e}_\phi)$, where $\mathbf{e}_\phi$ is the azimuthal normal vector. The next column corresponds to the local elongation rate. Thanks to the axisymmetry of the system (no velocity along the orthoradial direction, no dependence of the velocity components with the angular variable), the rate-of-deformation tensor can be written in the following way:

$$2\mathbf{E} = \boldsymbol{\nabla}\mathbf{v} + \boldsymbol{\nabla}\mathbf{v}^T = \begin{pmatrix} 2\dfrac{\partial v_r}{\partial r} & 0 & \dfrac{\partial v_z}{\partial r}+\dfrac{\partial v_r}{\partial z} \\ 0 & 2\dfrac{v_r}{r} & 0 \\ \dfrac{\partial v_z}{\partial r}+\dfrac{\partial v_r}{\partial z} & 0 & 2\dfrac{\partial v_z}{\partial z} \end{pmatrix}. \tag{15}$$

The eigenvalues of this tensor represent the local deformation (elongations and contractions) of a fluid element. The

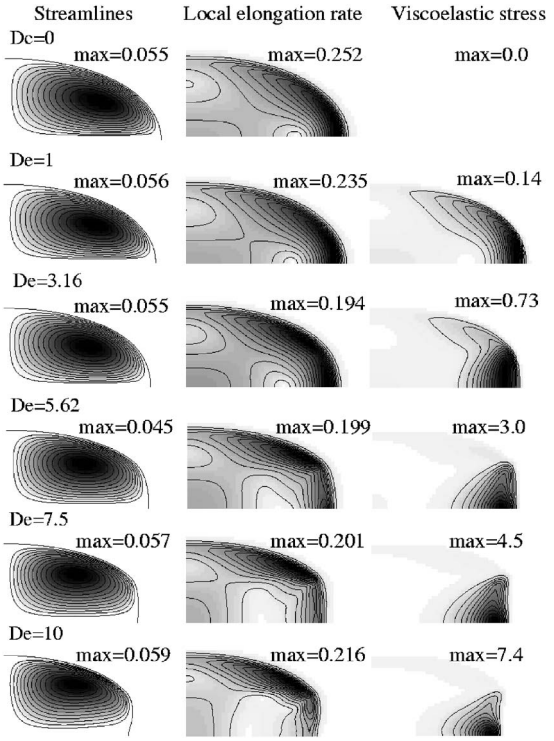

FIG. 6. Streamlines, local elongation rate, and viscoelastic stress for increasing values of De and for $Ca=0.1125$ (only a quarter of the drop is plotted).

sum of these three eigenvalues can be checked to be everywhere equal to 0, as expected from the incompressibility constraint (7). The local elongation rate can be estimated by computing the root mean square of the eigenvalues: $\sqrt{\mathrm{tr}\{\mathbf{E}\cdot\mathbf{E}^T\}}$; as a comparison, it would be equal to $\sqrt{3/2}\dot{\gamma}$ for a purely uniaxial elongation flow. This quantity is plotted in the second column of Fig. 6. The third column represents the viscoelastic stress as given by the trace of $\boldsymbol{\sigma}_p$. This quantity is directly related to the mean elongation of the polymers $\langle \mathbf{r}^2 \rangle$ through the relation [10]

$$\frac{\langle \mathbf{r}^2 \rangle}{\langle \mathbf{r}^2 \rangle_{eq}} = 1 + \frac{\mathrm{De}}{3\lambda_p}\mathrm{tr}(\boldsymbol{\sigma}_p). \tag{16}$$

Here, $\langle \mathbf{r}^2 \rangle_{eq}$ is the mean equilibrium end-to-end distance of the polymers, which is nonzero due to thermal forces.

Several interesting features can be observed in Fig. 6. First, the flow lines that occupy all the drop volume in the Newtonian situation tend to concentrate in the vicinity of the interface when the Deborah number increases. The flow is clockwise and the maximum value of the streamfunction ψ, indicated on the graph, corresponds to the intensity of the rotational flow. This intensity reaches a maximum for De $\simeq 1$ and decreases at larger values, indicating a strong viscoelastic screening of the flow. Note that ψ is defined such that $\psi=0$ along the contour of the drop (we checked that $\psi=0$ corresponds to the isocontour $\theta=0$ of the phase field, confirming the stationarity of the shape). From the deformation tensor, the local elongation rate can be computed as explained above and its localization illustrates quite well this phenomenon while increasing De. At low Deborah number the elongation rate is maximal at the tip of the drop. This can be easily understood since the capillary constraints are maximal at the tip and the counterflow induced by these constraints is thus very large in this region. This effect is amplified by the axial geometry since the flow has to converge towards the axis before going back to the central part of the drop. When the Deborah number is increased, the elongation rate at the tip decreases and the flow is displaced to the neighboring region, closer to the interface as also observed in [12] with the CR model. To understand this feature, it is interesting to consider the case of a single polymer placed in a Newtonian drop. For a Newtonian drop, the tip corresponds to the region where the elongation rate is maximum. A polymer present in the drop should follow the flow lines and rotate clockwise for the quarter of the drop considered in Fig. 6. If the polymer follows a streamline close to the interface of the drop it should suffer an increasing elongation rate before reaching the tip. While arriving close to the tip the polymer thus presents an elongation that should be relaxed on its way back to the central part of the drop, in the axial region of the drop. Not surprisingly, the viscoelastic stress plotted in the third column is essentially localized around the tip, where the polymers are expected to present the largest deformations. On its way to the tip, the polymer stores elastic energy while flowing in the vicinity of the interface where the elongation rate is large (after Fig. 6), resulting in the screening of the flow. Since the response of the polymer is delayed by a time τ, the screening becomes efficient mostly in the axial region of the drop explaining the strong damping of the flow there. The flow thus tends to escape from the axial region, amplifying the effect. Thanks to the localization of the viscoelastic stress at the tip, the capillary constraints are reduced since the polymers support part of the stress applied by the external elongation flow. The local curvature of the interface is thus reduced at the tip when viscoelastic effects are increased. Amazingly, at a large value of the Deborah number (De $\simeq 10$), the energy storage in the polymer solution seems to be so large that the curvature of the tip can even become negative. This kind of morphology has indeed already been observed in a similar system [35]: a macroscopic drop (of typical radius 1 cm, Newtonian or viscoelastic) is falling in a viscous fluid, and a stationary state is reached after a short time, depending on the density difference between the drop and the suspending fluid. Locally, at the rear side of the drop, the flow is fully similar to the one produced by the elongation (axisymmetry of the system and recirculations caused by the absence of normal velocities across the interface). In the case of the falling drop, a dimple appears at the rear of the viscoelastic drop, whereas the Newtonian remains nearly spherical. In this configuration, a stable torus can even appear, but in our situation, the drop loses its stability before any structure of this kind can be observed.

III. BURST

We consider here the burst transition that occurs when the applied stress overcomes the resistance of the drop (mainly

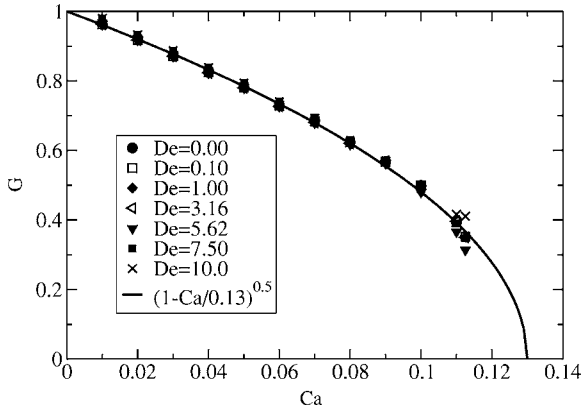

FIG. 7. Gaussian curvature in the mid section of the drop. The black curve is a parabolic fit of the whole set of data.

due to surface tension and viscoelasticity). The burst threshold is defined as the critical capillary number above which no steady shape can be defined. Above this threshold, the drop elongates until it breaks into smaller fragments. Although the burst threshold depends on the viscosity ratio λ, we shall not consider the dependence as a function of this parameter here, but restrict the discussion to $\lambda=1$. The main control parameter is thus the Deborah number De. As mentioned in the paper of Buckmaster and Flaherty [36] which devoted to the study of bursting of two-dimensional Newtonian droplets, a good criterion for the loss of stability is the cancelation of the curvature of the drop at its mid section. In three dimensions, the corresponding parameter should be the Gaussian curvature G which is defined as the product of the two local main curvatures κ_1 and κ_2 ($G=1$ for a sphere). Indeed, when the drop is locally cylindrical in its central region, the Gaussian curvature vanishes. This quantity is known to play an important role in surface topology, thanks to the Gauss-Bonnet theorem: the topological genus of a surface is equal to the integral of the Gaussian curvature over the whole surface, divided by 2π. We show in Fig. 7 the local Gaussian curvature in the mid section of the drop in the steady state for different values of De and Ca. Interestingly these curves are essentially insensitive to De, and can be fitted with a simple parabolic law (the continuous line of Fig. 7),

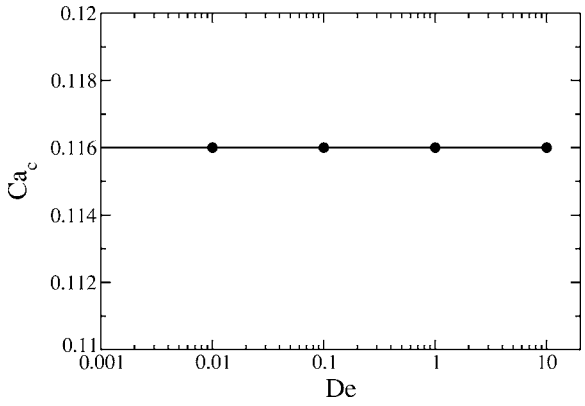

FIG. 8. Breakup threshold as a function of the Deborah number.

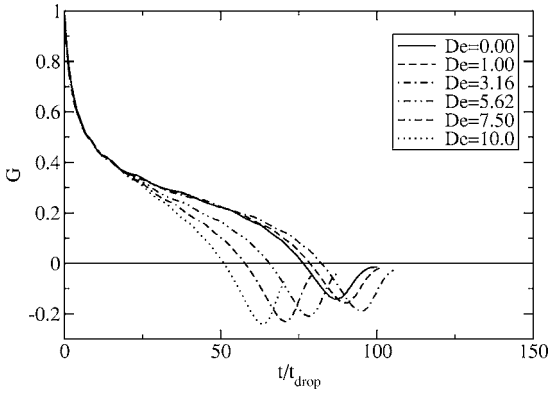

FIG. 9. Gaussian curvature in the mid section as a function of time during the burst (Ca=0.12).

$$G=\sqrt{1-\frac{\mathrm{Ca}}{\mathrm{Ca}_c}}, \tag{17}$$

where Ca_c corresponds to the cancellation of G, and should correspond to the 3D burst threshold after [36]. The critical capillary number Ca_c derived from this procedure is around 0.13 (close to 0.116, as determined below). The Gaussian curvature thus appears as a good parameter for the characterization of the transition. A more precise determination of the burst threshold can be achieved by using a dichotomic process on Ca, up to a relative precision of 10^{-3}.

The results are presented in Fig. 8. We found a critical capillary number $\mathrm{Ca}_c\sim 0.116$: up to this precision, no difference can be made between the different drops: viscoelasticity does not seem to play any major role in that process, as expected from Fig. 7, in agreement with [11]. This result can be understood by remembering that the viscoelastic effects are mainly located at the tip of the drop in the steady state, where elongation and contraction of the polymers are the most important, whereas the burst criterion is determined by the central part where elastic effects are weak. On the contrary, the burst dynamics (and thus the breakup) is affected by the presence of polymers, as can be seen in Fig. 9, where we have plotted the Gaussian curvature in the mid section as a function of time for different values of De. The Gaussian curvature is initially equal to unity, as expected from the spherical initial configuration (with $R=1$), and it decreases as time elapses. The curvature vanishes when the drop flattens in the middle, goes through a minimum, and tends toward zero, which corresponds to the Gaussian curvature of a cylinder. Another criterion for the burst is the relative elongation L/R of the drop (see Fig. 10). We see that this quantity increases very rapidly during the burst, with the presence of an inflexion point. These two points [first cancelation of G and $(d^2L/R)/dt^2=0$] will be used to quantify and compare the breakup velocity.

We show in Fig. 11 the value of these two breakup times for different Deborah numbers. Clearly, the general evolution of these two parameters is similar: at low De the burst mechanism is slowed down due to the presence of polymers, since the two curves are initially growing with De. Above a certain value of De, typically between 3 and 5, the dynamics

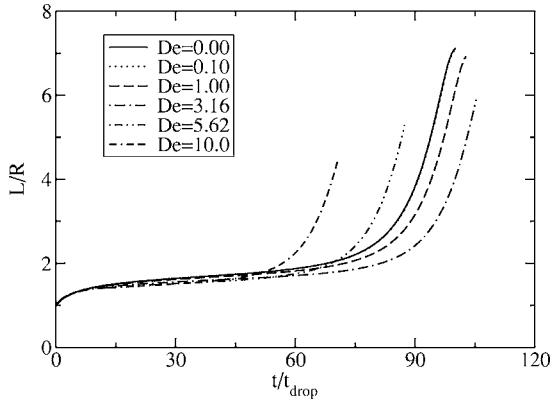

FIG. 10. Elongation of the drops as a function of time during the burst (Ca=0.12).

is suddenly accelerated, and becomes even faster than in the Newtonian case. This range of De was already mentioned in the previous section as the region where a dimple appears at the edges of the stationary shapes.

As an illustration, the burst dynamics is presented in Fig. 12 for a Newtonian drop (De=0) and for De=10, corresponding to the most viscoelastic situation considered here. The burst sequence is sampled every $10t_{drop}$ in this figure, so that the successive shapes presented by the Newtonian and the viscoelastic drops can be compared at equal time. We clearly observe a faster dynamics when De=10. The streamlines in the vicinity of the drop, the local strain rate, and the viscoelastic stress are shown in Fig. 13. The instantaneous streamlines can cross the interface since we consider unsteady flows, and we chose to present the streamlines going inside the drop only. We can observe that until $t \simeq 40t_{drop}$ a rotational counterflow is present inside the drop (the closed streamlines) while above $t=50t_{drop}$ the flow is essentially dominated by the imposed elongation. This feature illustrates that at the beginning, the drop resists quite efficiently against the elongational process, as shown in Fig. 10 where we can see that the deformation is slowed down until $t \simeq 40t_{drop}$. At later times, the deformation is accelerated again since the counterflow becomes too weak to compensate the applied elongation. We can further observe that between $t=50t_{drop}$ and $t=60t_{drop}$ a curvature inversion takes place at the tip (see

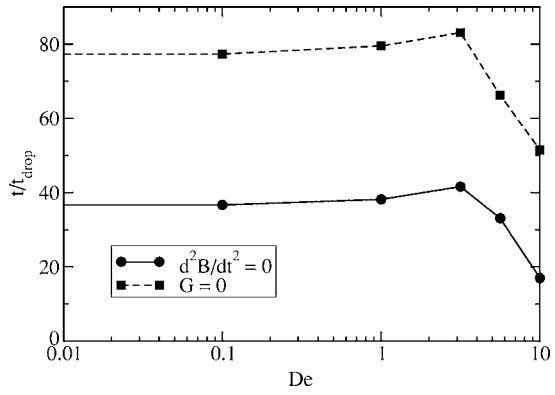

FIG. 11. Burst dynamics as measured by the breakup time (Ca=0.12).

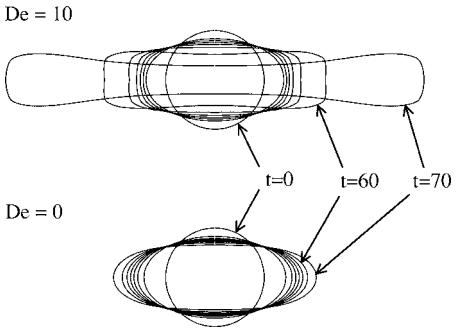

FIG. 12. Comparison of the burst dynamics for De=10 (top sequence) and for a Newtonian drop (bottom). The configurations are sampled every $10t_{drop}$(Ca=0.12). Time is mentioned in units of t_{drop} for $t=0$, 60, and 70. We clearly observe a faster dynamics when De=10.

Fig. 14), reminiscent of the counterflow and the growth of the viscoelastic stress located at the tip (last column of Fig. 13). The curvature inversion disappears at later stages as confirmed by the sudden reduction of the viscoelastic stress at the tip.

Above $t=60t_{drop}$ we can see in the second column of Fig. 13 that quite a large strain rate is applied to the center of the drop now, which strongly differs from the steady situation, and from the first stage of the burst (below the inflexion point in Fig. 10). Although we were not able to follow the dynamics above $t=75t_{drop}$, due to the extremely fast response, we can conjecture that this very large elongation rate in the central part of the drop should result in an accumulation of viscoelastic stress in this region. This building of the viscoelastic stress in the center of the drop is already visible in the last column of Fig. 13 for $t=70t_{drop}$. The presence of this stress should strongly alter the breakup sequence, and might even result in the production of a thin filament. Unfortunately, we could not reach the breakup itself for this

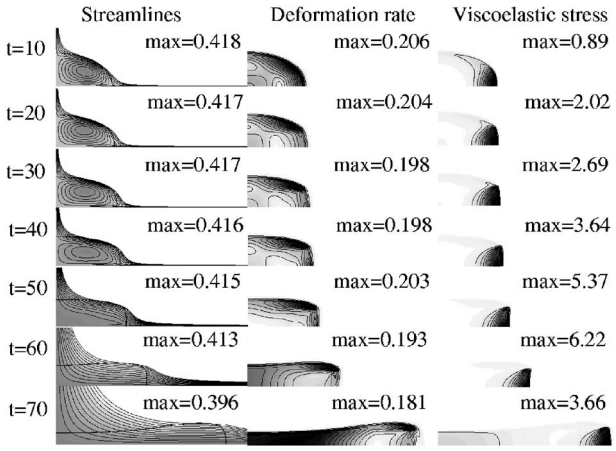

FIG. 13. Burst dynamics for De=10 and Ca=0.12. The streamlines are presented in the first column at different reduced times; the strong line corresponds to the instantaneous shape of the drop. The maximum value of the streamfunction is indicated at each time. The second column corresponds to the local deformation rate while the last column shows the location of the viscoelastic stress.

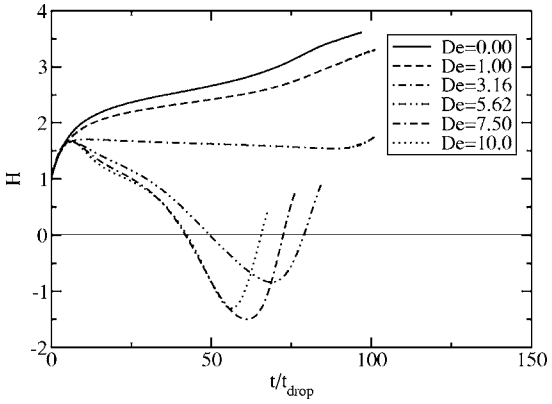

FIG. 14. Mean curvature at the tip of the drop during the burst. When $De \leqslant 5.62$, a transient curvature inversion is observed at the tip.

kind of applied flow, but there are strong indications that breakup is unlikely to occur in an Oldroyd-B fluid [37].

IV. CONCLUSION

The dynamical behavior of an isolated viscoelastic drop in a hyperbolic flow has been investigated using a phase field approach of the free boundary problem. We have shown that the method allows for the determination of the stationary shapes as well as the burst mechanisms. In the first case, we have shown that viscoelasticity induces morphological changes at the ends of the drop, along the main axis of elongation. A simple phenomenological mechanism involving a competition among the applied deformation, capillary effects, and viscoelasticity has been proposed in order to explain the dimple formation.

We have shown that the viscoelastic stress is mainly located at the ends of the drop in the stationary regime, and in the vicinity of the interface. This region corresponds to important recirculation processes. The burst transition corresponds to the loss of stability of the steady shape, and seems to be controlled by the central region of the drop. Indeed, the burst corresponds to the cancellation of the Gaussian curvature at the mid section of the drop. Since the central region of the drop corresponds to weak elastic constraints, the breakup threshold is found to be insensitive to elasticity (for Deborah numbers between 0 and 10), in agreement with previous results [11].

Finally, we have investigated the burst mechanism itself by considering a drop with $Ca > Ca_c(Ca=0.12)$ and we have shown that a good parameter to quantify the breakup velocity is either the time when the Gaussian curvature vanishes or when the second time derivative of $L(t)/R$ vanishes. The Gaussian curvature is, in our opinion, a better parameter since it can be measured on a single snapshot, while the inflexion point requires the measurement of the full elongation curve. These two parameters revealed that the breakup is first slowed down by viscoelasticity at low values of De (typically less than 3), and then suddenly accelerated. Once again, we proposed a simple explanation of this behavior by considering the location of the viscoelastic stress inside the drop. During the burst, the viscoelastic stress becomes important in the middle of the drop that should result in the formation of a thin filament.

Nevertheless, some important points still remain to be investigated. First of all, we know that the breakup threshold for Newtonian drops is affected by the viscosity ratio. The influence of this parameter in the viscoelastic case still needs to be considered. Some experimental studies [38] suggest that the threshold is only slightly affected when the viscosity ratio is larger than 1, but is considerably reduced when this parameter becomes small and that pointed unstable droplets are obtained. We are currently working in this direction. Second, the possible adsorption of polymers at the interface is expected to modify the dynamics of the drop and, for example, to induce ejection of microscopic droplets at its pointed edges [5]. This effect could be accounted for in principle in our model, and special attention should be paid to the precise modeling of Marangoni effects.

APPENDIX: NUMERICAL IMPLEMENTATION OF THE PHASE FIELD METHOD

We describe here the numerical scheme used to solve the phase field equations. Once the velocity field $\mathbf{v}$, the phase field θ, and the viscoelastic stress tensor $\boldsymbol{\sigma}_p$ are known at time t , a basic step consists in estimating their new values at time $t+dt$. We will establish the expressions for $\mathbf{v}^{t+dt}$, θ^{t+dt}, and $\boldsymbol{\sigma}_p^{t+dt}$ from Eqs. (13), and we shall explain how the various quantities involved in these expressions are computed, with special attention to the axisymmetrical nature of the system.

1. The velocity field

The Stokes equation (12) is solved using a relaxation method:

$$Re_n \partial_t \mathbf{v} = \boldsymbol{\nabla} \cdot \left(\frac{1-\theta}{2} \boldsymbol{\sigma}_{s,i} + \frac{1+\theta}{2} \boldsymbol{\sigma}_{s,o} + \boldsymbol{\sigma}_p \right) - \boldsymbol{\nabla} P - c[\theta] \boldsymbol{\nabla} \theta. \tag{A.1}$$

Re_n is a numerical Reynolds number which controls the relaxation velocity. In practice, this parameter is of order 10^{-2} in order to stay in the Stokes regime. Equation (A.1) can be rewritten as

$$\mathrm{Re}_n \partial_t \mathbf{v} = \lambda_s[\theta] \Delta \mathbf{v} - \boldsymbol{\nabla} P - c[\theta] \boldsymbol{\nabla} \theta + \boldsymbol{\nabla} \cdot \boldsymbol{\sigma}_p + \lambda_s'[\theta] \boldsymbol{\nabla} \theta \cdot (\boldsymbol{\nabla} \mathbf{v} + \boldsymbol{\nabla} \mathbf{v}^T), \tag{A.2}$$

with $\lambda_s[\theta] = [(1-\theta)/2]\lambda_s + (1+\theta)/2$ and $\lambda_s'[\theta] = d\lambda_s[\theta]/d\theta$. We have used the incompressibility constraint (7) to eliminate the term $\boldsymbol{\nabla} \cdot (\boldsymbol{\nabla} \mathbf{v}^T) = \boldsymbol{\nabla} (\boldsymbol{\nabla} \cdot \mathbf{v}) = 0$. Thanks to the axisymmetric geometry of the system, the resolution can be performed in 2D. In cylindrical coordinates the rate-of-deformation tensor is given by

$$\mathbf{D} = \nabla \mathbf{v} + \nabla \mathbf{v}^T = \begin{pmatrix} 2\frac{\partial v_r}{\partial r} & 0 & \frac{\partial v_z}{\partial r} + \frac{\partial v_r}{\partial z} \\ 0 & 2\frac{v_r}{r} & 0 \\ \frac{\partial v_z}{\partial r} + \frac{\partial v_r}{\partial z} & 0 & 2\frac{\partial v_z}{\partial z} \end{pmatrix} \tag{A.3}$$

so the contribution $\nabla\theta\cdot(\nabla\mathbf{v}+\nabla\mathbf{v}^T)$ appearing in Eq. (A.2) reduces to

$$\nabla\theta\cdot(\nabla\mathbf{v}+\nabla\mathbf{v}^T) = \begin{pmatrix} 2\frac{\partial\theta}{\partial r}\frac{\partial v_r}{\partial r} + \frac{\partial\theta}{\partial z}\left(\frac{\partial v_r}{\partial z} + \frac{\partial v_z}{\partial r}\right) \\ 0 \\ \frac{\partial\theta}{\partial r}\left(\frac{\partial v_r}{\partial z} + \frac{\partial v_z}{\partial r}\right) + 2\frac{\partial\theta}{\partial z}\frac{\partial v_z}{\partial z} \end{pmatrix}. \tag{A.4}$$

The Laplace operator for a vector field is given by

$$\Delta\mathbf{v} = \begin{pmatrix} \frac{\partial^2 v_r}{\partial r^2} + \frac{\partial^2 v_r}{\partial z^2} + \frac{\partial}{\partial r}\left(\frac{v_r}{r}\right) \\ 0 \\ \frac{\partial^2 v_z}{\partial r^2} + \frac{\partial^2 v_z}{\partial z^2} + \frac{1}{r}\frac{\partial v_z}{\partial r} \end{pmatrix}, \tag{A.5}$$

where we have explicitly assumed an axisymmetrical geometry. This expression only differs from a 2D Laplacian by the extra $1/r$ contribution. Equation (A.2) can thus be rewritten as

$$\mathrm{Re}_n\partial_t\mathbf{v} = \lambda_s[\theta]\Delta_{2D}\mathbf{v} - \nabla P + \mathbf{F} \tag{A.6}$$

with

$$\mathbf{F} = -c[\theta]\nabla\theta + \nabla\cdot\boldsymbol{\sigma}_p + \lambda_s'[\theta]\nabla\theta\cdot(\nabla\mathbf{v}+\nabla\mathbf{v}^T) + \lambda_s[\theta]\begin{pmatrix} \frac{\partial}{\partial r}\left(\frac{v_r}{r}\right) \\ \frac{1}{r}\frac{\partial v_z}{\partial r} \end{pmatrix} \tag{A.7}$$

and

$$\Delta_{2D}\mathbf{v} = \begin{pmatrix} \frac{\partial^2 v_r}{\partial r^2} + \frac{\partial^2 v_r}{\partial z^2} \\ \frac{\partial^2 v_z}{\partial r^2} + \frac{\partial^2 v_z}{\partial z^2} \end{pmatrix}. \tag{A.8}$$

The computation of $\mathbf{F}$ is straightforward once $\boldsymbol{\sigma}_p$ is known (see paragraph 3 below). The main difficulty concerns the computation of the curvature field, defined as $c[\theta]=\nabla\cdot\hat{\mathbf{n}}/2$ with $\hat{\mathbf{n}}=\nabla\theta/|\nabla\theta|$. Although $\nabla\theta$ corresponds exactly to the 2D expression in the (r,z) space, the divergence itself is slightly modified and is written as

$$\nabla\cdot\mathbf{v} = \nabla_{2D}\cdot\mathbf{v} + \frac{v_r}{r}, \tag{A.9}$$

with $\nabla_{2D}\cdot\mathbf{v}=(\partial v_r/\partial r)+(\partial v_z/\partial z)$ the usual two-dimensional divergence.

In all these expressions, the $1/r$ contributions require special care at $r=0$. The divergence is indeed artificially introduced by the coordinate system and the physical quantities entering in the problem have a regular behavior on the axis. A simple extrapolation scheme can thus be used to estimate these quantities at $r=0$. We used the third order extrapolation scheme,

$$f(0) = \frac{1}{11}[18f(dr) - 9f(2dr) + 2f(3dr)] \tag{A.10}$$

with dr the mesh size in the radial direction. Written in this way, the system can be treated as purely two dimensional.

The $\Delta_{2D}\mathbf{v}$ term in Eq. (A.6) is known to introduce numerical instabilities when the time step is too large. Two possibilities exist to suppress this problem: reducing the time step or using an implicit scheme. The second solution is much more powerful since it fully suppresses the instability. However, we cannot use this scheme here in a strict way due to the non linearity introduced by the spatial variation of the viscosity field $\lambda_s[\theta]$. A mixed scheme can be implemented by subtracting $\lambda_{s,max}\Delta_{2D}\mathbf{v}$ from both sides of Eq. (A.6), where $\lambda_{s,max}$ is the largest value of the viscosity in the system. Equation (A.6) is therefore rewritten as

$$\left[\mathrm{Re}_n\frac{\partial}{\partial t} - \lambda_{s,max}\Delta_{2D}\right]\mathbf{v} = (\lambda_s[\theta] - \lambda_{s,max})\Delta_{2D}\mathbf{v} - \nabla P + \mathbf{F}. \tag{A.11}$$

Although we use in practice a fourth order Runge-Kutta method for the temporal integration, it is interesting to consider a single semi-implicit Euler integration step to emphasize the interest of Eq. (A.11). The temporal derivation can be discretized as $\partial\mathbf{v}/\partial t \sim (\mathbf{v}^{t+dt}-\mathbf{v}^t)/dt$, where dt is the time step, and then Eq. (A.11) takes the discrete form

$$\mathrm{Re}_n\frac{\mathbf{v}^{t+dt}-\mathbf{v}^t}{dt} - \lambda_{s,max}\Delta_{2D}\mathbf{v}^{t+dt} = (\lambda_s[\theta^t] - \lambda_{s,max})\Delta_{2D}\mathbf{v}^t - \nabla P + \mathbf{F}^t. \tag{A.12}$$

The implicit method consists of evaluating the Laplacian term on the left side at time $t+dt$. The velocity field at time $t+dt$ is then obtained by inverting

$$\left(1 - \lambda_{s,max}\frac{dt}{\mathrm{Re}_n}\Delta_{2D}\right)\mathbf{v}^{t+dt} = \mathbf{v}^t + \frac{dt}{\mathrm{Re}_n}\{(\lambda_s[\theta] - \lambda_{s,max})\Delta_{2D}\mathbf{v} - \nabla P + \mathbf{F}\}^t. \tag{A.13}$$

This inversion can easily be done in the (spatial) Fourier space if periodic boundary conditions (PBC) apply at the edge of the resolution box. This is indeed not the case in general when the drop is placed in an external flow, like a hyperbolic elongation, for example. Interestingly, if the external applied flow is linear (this is indeed the case for the

applied elongation flow), the only contribution arises in the rate-of-deformation tensor, not in the Laplacian, and can be evaluated analytically. Setting $\mathbf{v}=\mathbf{v}_i+\mathbf{u}$, where the imposed field $\mathbf{v}_i$ is time independent and linear in space, and $\mathbf{u}$ is the velocity field induced by the drop, Eq. (A.13) rewrites

$$\left(1-\lambda_{s,max}\frac{dt}{\mathrm{Re}_n}\Delta_{2D}\right)\mathbf{u}^{t+dt}=\mathbf{u}^t+\frac{dt}{\mathrm{Re}_n}\{(\lambda_s[\theta]-\lambda_{s,max})\Delta_{2D}\mathbf{u}-\boldsymbol{\nabla}P+\mathbf{F}\}^t. \tag{A.14}$$

Assuming PBC for the induced field $\mathbf{u}$ only, and noticing that the gradient tensor only plays a role in the vicinity of the interface thanks to the $\boldsymbol{\nabla}\theta$ prefactor [see Eq. (A.7)], this contribution cancels at the boundary of the resolution box and can then satisfy PBC. This last equation can thus be inverted in the Fourier space to give

$$\mathbf{u}_k^{t+dt}=\frac{1}{1+\lambda_{s,max}\frac{dt}{\mathrm{Re}_n}k^2}\times\left[\mathbf{u}_k^t+\frac{dt}{\mathrm{Re}_n}\{(\lambda_s[\theta]-\lambda_{s,max})\Delta_{2D}\mathbf{u}-\boldsymbol{\nabla}P+\mathbf{F}\}_k^t\right] \tag{A.15}$$

where index "k" denotes a spatial Fourier transformation of the quantity at wavevector k. The power of the implicit scheme comes from the property that $|1/[1+\lambda_{s,max}(dt/\mathrm{Re}_n)k^2]|\leqslant 1$ for all wavevectors k whatever the value of dt, which ensures the stability of the iterative scheme in the absence of the term between braces (pure diffusion). Due to the presence of this extra term, the iterative scheme does not always converge, but instabilities occur at much larger values of dt.

In this equation, the pressure field P is determined by the incompressibility condition

$$\boldsymbol{\nabla}\cdot\mathbf{v}=0. \tag{A.16}$$

A recursive procedure has been implemented in order to determine P. Equation (A.15) is used without the pressure term to determine an auxiliary velocity field $\tilde{\mathbf{u}}_k^{t+dt}$:

$$\tilde{\mathbf{u}}_k^{t+dt}=\frac{1}{1+\lambda_{s,max}\frac{dt}{\mathrm{Re}_n}k^2}\times\left[\mathbf{u}_k^t+\frac{dt}{\mathrm{Re}_n}\{(\lambda_s[\theta]-\lambda_{s,max})\Delta_{2D}\mathbf{u}+\mathbf{F}\}_k^t\right]. \tag{A.17}$$

The recursive procedure

$$P_k=P_k-dt_P\{\boldsymbol{\nabla}\cdot\mathbf{u}\}_k,$$

$$\mathbf{u}_k^{t+dt}=\tilde{\mathbf{u}}_k^{t+dt}+\frac{1}{1+\lambda_{s,max}\frac{dt}{\mathrm{Re}_n}k^2}\{\boldsymbol{\nabla}P\}_k \tag{A.18}$$

(with dt_P an auxiliary time step) is then iterated until the mean value of the absolute value of $\boldsymbol{\nabla}\cdot\mathbf{u}$ is less than 10^{-5} in the Fourier space. The final pressure field is then stored and used as the starting point for the next time step. After some time steps, the number of iterations of procedure (A.18) is reduced to 1 or 2, and the global iteration is then considerably accelerated. Finally, a backward Fourier transformation and the addition of the applied velocity field leads to the new velocity field $\mathbf{v}^{t+dt}$.

2. The phase field

The phase field equation is given by

$$\frac{\partial\theta}{\partial t}=-\mathbf{v}\cdot\boldsymbol{\nabla}\theta+\frac{1}{\Gamma}\left(-\frac{\delta\mathcal{F}}{\delta\theta}-2c\epsilon^2|\boldsymbol{\nabla}\theta|\right) \tag{A.19}$$

with $\mathcal{F}=\int\{(1-\theta^2)^2/4+\epsilon^2(\boldsymbol{\nabla}\theta)^2/2\}d\mathbf{r}$, so that Eq. (A.19) becomes

$$\frac{\partial\theta}{\partial t}=-\mathbf{v}\cdot\boldsymbol{\nabla}\theta+\frac{1}{\Gamma}\{\theta(1-\theta^2)+\epsilon^2(\Delta\theta-2c|\boldsymbol{\nabla}\theta|)\}. \tag{A.20}$$

Once again, numerical difficulties due to the Laplacian term can be expected in principle at large time steps, but thanks to the prefactor ϵ^2/Γ this contribution remains small enough so that a standard explicit Euler scheme is sufficient:

$$\theta^{t+dt}=\theta^t+dt\left[-\mathbf{v}\cdot\boldsymbol{\nabla}\theta+\frac{1}{\Gamma}\{\theta(1-\theta^2)+\epsilon^2(\Delta\theta-2c|\boldsymbol{\nabla}\theta|)\}\right]^t. \tag{A.21}$$

As for the velocity field, this elementary step is included in a fourth order Runge-Kutta method.

3. The constitutive equation

The dimensionless Oldroyd-B equation is given by

$$\mathrm{De}\frac{1-\theta}{2}\left(\frac{\partial\boldsymbol{\sigma}_p}{\partial t}+\mathbf{v}\cdot\boldsymbol{\nabla}\boldsymbol{\sigma}_p-\boldsymbol{\nabla}\mathbf{v}^T\cdot\boldsymbol{\sigma}_p-\boldsymbol{\sigma}_p\cdot\boldsymbol{\nabla}\mathbf{v}\right)+\boldsymbol{\sigma}_p=\lambda_p\frac{1-\theta}{2}(\boldsymbol{\nabla}\mathbf{v}+\boldsymbol{\nabla}\mathbf{v}^T). \tag{A.22}$$

For the sake of simplicity, we shall write $\tilde{\mathrm{De}}=\mathrm{De}(1-\theta)/2$ and $\tilde{\lambda}_p=\lambda_p(1-\theta)/2$. This equation is discretized in time similar the previous ones and we use an implicit scheme to compute $\boldsymbol{\sigma}_p$ at time $t+dt$:

$$\boldsymbol{\sigma}_p^{t+dt}=\frac{\tilde{\mathrm{De}}}{\tilde{\mathrm{De}}+dt}[\boldsymbol{\sigma}_p^t-dt\mathbf{v}^t\boldsymbol{\nabla}\boldsymbol{\sigma}_p^t+dt(\boldsymbol{\nabla}\mathbf{v}^T\cdot\boldsymbol{\sigma}_p^t-\boldsymbol{\sigma}_p^t\cdot\boldsymbol{\nabla}\mathbf{v})]+\frac{\tilde{\lambda}_p dt}{\tilde{\mathrm{De}}+dt}(\boldsymbol{\nabla}\mathbf{v}+\boldsymbol{\nabla}\mathbf{v}^T). \tag{A.23}$$

Once again, the implicit treatment consists of evaluating $\boldsymbol{\sigma}_p$ on the left-hand-side of Eq. (A.23) at time $t+dt$, where t and dt are dimensionless. Using this approach, the case $\tilde{\mathrm{De}}=0$

does not require any special treatment. The Newtonian case is then simply recovered since we have in this case

$$\boldsymbol{\sigma}_p^{t+dt} = \tilde{\lambda}_p(\boldsymbol{\nabla}\mathbf{v} + \boldsymbol{\nabla}\mathbf{v}^T). \quad \text{(A.24)}$$

Moreover, this equation is valid everywhere in space since the case $\theta=1$ (outside the drop), and then De=1, is not singular. This elementary step is then also included in a fourth order Runge-Kutta method.

4. Numerical parameters

The resolution is performed on a rectangular grid of size $N_Z \times N_R$, where N_Z is the number of grid points in the axial direction z, and N_R is the number of grid points in the radial direction r. While $N_R=250$, N_Z varies between 300 and 1000, depending on the drop extension. The unit cell is chosen to be a square ($dr=dz=0.03\,R$, where R is the radius of the drop at rest). The phase field interfacial width ϵ is fixed to $\epsilon=dr=dz$ and the relaxation time Γ introduced in the phase-field equation (A.19) coincides with t_{drop}. The time step used for the dynamical solution is $dt=10^{-2}t_{drop}$.

[1] G. I. Taylor, Proc. R. Soc. London, Ser. A **138**, 41 (1932).
[2] R. G. Cox, J. Fluid Mech. **37**, 601 (1969).
[3] D. Barthès-Biesel and A. Acrivos, J. Fluid Mech. **61**, 1 (1973).
[4] J. M. Rallison, Annu. Rev. Fluid Mech. **16**, 45 (1995).
[5] H. A. Stone, Annu. Rev. Fluid Mech. **26**, 65 (1994).
[6] J. G. Oldroyd, Proc. R. Soc. London, Ser. A **218**, 122 (1953).
[7] J. G. Oldroyd, Proc. R. Soc. London, Ser. A **232**, 567 (1955).
[8] J. F. Palierne, Rheol. Acta **29**, 204 (1990).
[9] I. Delaby, B. Ernst, D. Froelich, and R. Muller, Polym. Eng. Sci. **36**, 1627 (1996).
[10] R. B. Bird, R. C. Armstrong, and R. A. Brown, *Dynamics of Polymeric Liquids* (Wiley, New York, 1977), Vol. 1.
[11] P. L. Maffettone and F. Greco, J. Rheol. **48**, 83 (2004).
[12] S. Ramaswamy and L. G. Leal, J. Non-Newtonian Fluid Mech. **85**, 127 (1999).
[13] T. Biben, C. Misbah, A. Leyrat, and C. Verdier, Europhys. Lett. **63**, 623 (2003).
[14] R. Hooper, M. Toose, C. W. Macosko, and J. J. Derby, Int. J. Numer. Methods Fluids **37**, 837 (2001).
[15] R. Hooper, V. F. de Almeida, C. W. Macosko, and J. J. Derby, J. Non-Newtonian Fluid Mech. **98**, 141 (2001).
[16] J. B. Collins and H. Levine, Phys. Rev. B **31**, 6119 (1985).
[17] R. Kobayashi, Physica D **63**, 410 (1993).
[18] A. Karma and W.-J. Rappel, Phys. Rev. Lett. **77**, 4050 (1996).
[19] K. Kassner and C. Misbah, Europhys. Lett. **46**, 217 (1999).
[20] R. Folch, J. Casademunt, A. Hernández-Machado, and L. Ramírez-Piscina, Phys. Rev. E **60**, 1724 (1999).
[21] R. Folch, J. Casademunt, A. Hernández-Machado, and L. Ramírez-Piscina, Phys. Rev. E **60**, 1734 (1999).
[22] R. Borcia and M. Bestehorn, Phys. Rev. E **67**, 066307 (2003).
[23] J. Beaucourt, F. Rioual, T. Séon, T. Biben, and C. Misbah, Phys. Rev. E **69**, 011906 (2004).
[24] T. Roths, C. Friedrich, M. Marth, and J. Honerkamp, Rheol. Acta **41**, 211 (2002).
[25] E. S. G. Shaqfeh, Annu. Rev. Fluid Mech. **28**, 129 (1996).
[26] R. G. Larson, *Constitutive Equations for Polymer Melts and Solutions* (Butterworth-Heinemann, (1988).
[27] L. Landau and E. Lifschitz, *Fluid Mechanics* (Pergamon Press, New York 1986).
[28] J. Eggers, Phys. Rev. Lett. **71**, 3458 (1993).
[29] I. Cohen, M. P. Brenner, J. Eggers, and S. R. Nagel, Phys. Rev. Lett. **83**, 1147 (1999).
[30] M. Renardy, J. Non-Newtonian Fluid Mech. **104**, 65 (2002).
[31] A. U. Chen, P. K. Notz, and O. A. Basaran, Phys. Rev. Lett. **88**, 174501 (2002).
[32] M. Goldin, J. Yerushalmi, R. Pfeffer, and R. Shinnar, J. Fluid Mech. **38**, 689 (1969).
[33] M. Sostarecz and A. Belmonte, Phys. Fluids **16**, L67 (2004).
[34] A spherical shape for the drop corresponds to $\theta(t=0) = \tanh[(d-R)/\sqrt{2}\epsilon]$ where $d=\sqrt{r^2+z^2}$ is the distance to the center, and ϵ is the width of the interface.
[35] M. Sostarecz and A. Belmonte, J. Fluid Mech. **497**, 235 (2002).
[36] J. D. Buckmaster and J. E. Flaherty, J. Fluid Mech. **60**, 625 (1972).
[37] W. J. Milliken and L. G. Leal, J. Non-Newtonian Fluid Mech. **40**, 355 (1991).
[38] M. Renardy, J. Non-Newtonian Fluid Mech. **51**, 97 (1994).